

Spatial distribution of heat flux and fluctuations in turbulent Rayleigh-Bénard convection

Rajaram Lakkaraju¹, Richard. J. A. M. Stevens¹, Roberto Verzicco^{1,2},
Siegfried Grossmann³, Andrea Prosperetti^{1,4}, Chao Sun¹, and Detlef Lohse¹

¹*Faculty of Science and Technology, Mesa+ Institute and J. M. Burgers Center for Fluid Dynamics,
University of Twente, 7500AE Enschede, The Netherlands*

²*Department of Mechanical Engineering, University of Rome 'Tor Vergata', Via del Politecnico 1, 00133 Rome, Italy*

³*Department of Physics, University of Marburg, Renthof 6, D-35032 Marburg, Germany and*

⁴*Department of Mechanical Engineering, Johns Hopkins University, Baltimore, MD 21218, USA*

(Dated: April 21, 2022)

We numerically investigate the radial dependence of the velocity and temperature fluctuations and of the time-averaged heat flux $\bar{j}(r)$ in a cylindrical Rayleigh-Bénard cell with aspect ratio $\Gamma = 1$ for Rayleigh numbers Ra between 2×10^6 and 2×10^9 at a fixed Prandtl number $Pr = 5.2$. The numerical results reveal that the heat flux close to the side wall is larger than in the center and that, just as the global heat transport, it has an effective power law dependence on the Rayleigh number, $\bar{j}(r) \propto Ra^{\gamma_j(r)}$. The scaling exponent $\gamma_j(r)$ decreases monotonically from 0.43 near the axis ($r \approx 0$) to 0.29 close to the side walls ($r \approx D/2$). The effective exponents near the axis and the side wall agree well with the measurements of Shang et al. (Phys. Rev. Lett. **100**, 244503, 2008) and the predictions of Grossmann and Lohse (Phys. Fluids **16**, 1070, 2004). Extrapolating our results to large Rayleigh number would imply a crossover at $Ra \approx 10^{15}$, where the heat flux near the axis would begin to dominate. In addition, we find that the local heat flux is more than twice as high at the location where warm or cold plumes go up or down, than in the plume depleted regions.

PACS numbers: 47.55.P-,47.55.pb,44.25.+f

I. INTRODUCTION

In Rayleigh-Bénard (RB) convection a fluid is heated from below and cooled from above. This problem of thermal convection is of the utmost importance from an applied point of view. Examples are thermal convection in the atmosphere, in the oceans and in process technology. For recent reviews of RB convection we refer to Refs. [1, 2].

In a cylindrical container, the dynamics of a RB system depends on three control parameters, the Rayleigh number $Ra = g\beta\Delta L^3/\nu\kappa$, the Prandtl number $Pr = \nu/\kappa$, and the aspect ratio $\Gamma = D/L$. Here g is the gravitational acceleration, β the isobaric thermal expansion coefficient, Δ the temperature difference between the top and bottom plates, ν the kinematic viscosity, κ the thermal diffusivity, and L and D are the height and diameter of the cylinder. The response of the system is expressed by the Nusselt number Nu , the dimensionless heat flux [1].

Previous studies mainly focused on determining the global heat flux as a function of Ra and Pr . For water ($Pr = 4 - 6$), in the experimentally available range of $Ra = 10^8 - 10^{11}$, one finds that the global heat transport effectively scales as $Nu \sim Ra^{0.29-0.31}$ [1, 3–8]. The effective exponents for the global heat flux are well described by the unifying theory of Refs. [4, 9–11]. That theory also made predictions for the scaling exponents of the local heat flux in the center of the cell and at the side wall [11]. The reasoning is based on splitting the thermal energy dissipation field into its plume and background contributions; similarly the kinetic energy dissipation is decomposed into its boundary layer and bulk

contributions. By doing this Grossmann and Lohse [11] accounted for the various scalings in the $Ra - Pr$ parameter space. They found that the local heat flux has an effective power law dependence on the Ra number, $\bar{j}(r) \propto Ra^{\gamma_j(r)}$, and obtained a prediction for the scaling exponent $\gamma_j = 0.45$ in the bulk (center) and $\gamma_j = 0.22$ at the plume (side wall) regions.

In order to understand the heat flux one has to either rely on Eulerian [12] or Lagrangian [13, 14] measurements where the complex interplay between velocity and temperature can be studied. Advancements in the experimental techniques made it possible to measure the vertical local velocity $u_z(\mathbf{r}, t)$ and the local temperature $T(\mathbf{r}, t)$ at a given spatial location \mathbf{r} as functions of time. This allowed Shang et al. [12, 15] to determine the local convective heat flux [16]

$$j(\mathbf{r}, t) = \frac{u_z(\mathbf{r}, t)[T(\mathbf{r}, t) - T_0]}{\kappa\Delta/L}, \quad (1)$$

where T_0 is the mean bulk temperature. They determined the probability density functions (PDF) of the local heat flux in the axis and side wall regions and showed that the vertical heat flux is highly non-Gaussian and intermittent due to thermal plumes. This work stimulated Ching et al. [17] to theoretically study the problem. They decomposed the velocity field into a part associated with strong temperature fluctuations plus a background and found that, with the definitions they used, the local heat transport associated with the former velocity component near the axis of the cell scaled as $Ra^{1/7}$. Later experiments by Shang et al. [18] revealed that the effective scaling exponent for the local heat flux is about

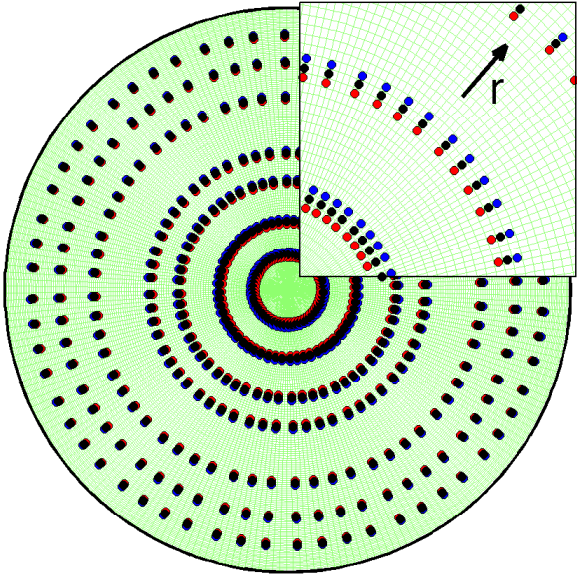


FIG. 1. Computational grid used for $Ra = 2 \times 10^7$. We position numerical probes uniformly in azimuthal direction in circles at seven radial locations $r/L = 0.06, 0.12, 0.19, 0.24, 0.34, 0.40, 0.45$ (shown in black). For better statistics we use two more sets of probes (blue, red) with an offset of one grid point. Inset shows a close up view of the probe locations on the grid.

0.49 near the cell axis and about 0.24 near the side wall, which confirms the main results obtained by Grossmann and Lohse [11], but is in disagreement with the model of Ching et al. [17].

In experiments it is quite difficult to measure the heat flux at each spatial point in the cell due to problems with measurement techniques and the presence of inherent noise levels. The measurements at just one or two points may not be enough to understand the complex dynamics involved in the convection process. The present paper offers numerical results which complement the work initiated by Shang et al. [12, 18]. We provide information on the heat flux at one quarter, one half, and three quarters of the cell height for several radial positions r , not only near the axis and the side wall. This information allows us to understand the two limits in the unifying theory [11] on the effective scaling exponents, one valid in the bulk (the central region of the cell) and the other valid in the plume region. As a result we clearly see persistence of the inhomogeneous nature of the flow in the radial direction which leads to different scaling exponents.

In experiments the local velocity is measured by LDV/PIV techniques at a spatial position which slightly differs from the location of the local temperature measurement. This spatial misalignment may possibly affect the results. In numerical simulations, in contrast, one has all the information on the flow field and thus the local heat flux can be calculated from the velocity and temperature measurements at exactly the same position.

Finally we comment on the local heat flux distribution with respect to the large scale circulation and the ultimate regime mentioned in Refs. [9, 11, 19] and provide data to illuminate the differences between the measurements of Shang et al. [18] and the earlier Ching et al. [17] claims.

In simulations the Ra number range and the duration available for time-averaging are more limited than in experiments. In order to mitigate the latter shortcoming we have limited the Ra number of our simulations. In the next section we briefly describe the numerical procedure before discussing our results on the local heat flux and the velocity and temperature fluctuations.

II. NUMERICAL METHOD

We performed direct numerical simulations for a Boussinesq fluid in a unit aspect ratio ($\Gamma = 1$) cylinder with constant temperatures applied at the top and bottom plates and an adiabatic side wall. The fluid simulated in our calculations is water at 32 °C ($Pr = 5.2$) for $2 \times 10^6 \leq Ra \leq 2 \times 10^9$. The governing equations for momentum, energy and mass conservation in dimensionless form are given by [20]

$$\frac{D\mathbf{u}}{Dt} = -\nabla p + \theta \hat{\mathbf{z}} + \left(\frac{Pr}{Ra}\right)^{1/2} \nabla^2 \mathbf{u}, \quad (2)$$

$$\frac{D\theta}{Dt} = \frac{1}{(PrRa)^{1/2}} \nabla^2 \theta, \quad \nabla \cdot \mathbf{u} = 0. \quad (3)$$

Here the dimensionless variables are the velocity \mathbf{u} , temperature θ and pressure p (minus the hydrostatic contribution). The material derivative is denoted by D/Dt . The unit vector $\hat{\mathbf{z}}$ is in the direction opposite to gravity. The physical variables such as length and velocity are made non-dimensional by the cylinder height (L), and the free-fall velocity $U = \sqrt{g\beta\Delta L}$. Constant dimensionless temperatures of 1 and 0 are applied at the bottom and top plate, respectively.

The governing equations are solved on a staggered grid with second-order accuracy in space and time. For the time advancement a third order Runge-Kutta scheme is used. This method is stable for a CFL number up to $\sqrt{3}$, and here we have limited it to 1.2 by adjusting the time step according to the maximum velocity before executing each time step [21]. More details about the numerical method can be found in Refs. [20, 22, 23]. For the spatial resolution we followed the criteria set by Stevens et al. [24].

A summary of the simulation parameters is shown in Table I. The first and second columns are Ra and the number of grid nodes. The volume- and time-averaged global heat transport, i.e. the Nusselt number $Nu = 1 + \sqrt{RaPr} \left[\overline{\langle u_z \theta \rangle_V} \right]$, is shown in the third column; here the overline denotes time averages and the angular brackets $\langle \cdot \rangle_V$ volume averages. The number of grid points used

TABLE I. Summary of simulation parameters: The number of grid points used in angular (N_ϕ), radial (N_r), and axial directions (N_z), volume and time averaged Nusselt number (Nu), the number of grid points in the thermal boundary layer (n_{bl}), convergence of exact relations for ε_K and ε_T , comparing maximum of grid spacing in angular ($\delta\phi_m$) and axial (δz_m) directions with the Kolmogorov length scale based on global kinetic energy dissipation rate (η) and the averaging time considered for the simulations are shown. The reported times are always measured in the units of free fall time and the lengths in terms of cylinder height. For statistical averages we discarded the initial 140 dimensionless times, to prevent transient effects in the results.

Ra	$N_\phi \times N_r \times N_z$	Nu	n_{bl}	$\frac{\varepsilon_K}{\frac{\nu^3}{L^4} \frac{Ra}{Pr^2} (Nu-1)}$	$\frac{\varepsilon_T}{\kappa \frac{\Delta^2}{L^2} Nu}$	$\delta\phi_m, \delta z_m, \eta$ ($\times 10^2$)	in L/U
2×10^6	$193 \times 49 \times 129$	10.93	19	1.008	0.968	2.26, 1.45, 3.41	4200
1×10^7	$257 \times 65 \times 193$	16.58	18	1.010	0.971	2.44, 0.73, 2.04	3700
2×10^7	$257 \times 65 \times 193$	20.71	18	1.007	0.843	2.44, 0.73, 1.62	3700
6×10^7	$321 \times 97 \times 239$	28.48	14	0.989	0.923	1.96, 0.97, 1.13	3000
1×10^8	$385 \times 129 \times 257$	33.25	15	0.997	0.955	1.62, 0.73, 0.95	2800
2×10^8	$385 \times 129 \times 257$	40.87	13	1.002	0.937	1.62, 0.73, 0.76	2700
5×10^8	$513 \times 161 \times 321$	52.80	13	1.005	0.947	1.22, 0.51, 0.56	1900
2×10^9	$769 \times 193 \times 385$	80.34	11	0.992	0.959	0.82, 0.34, 0.26	2040

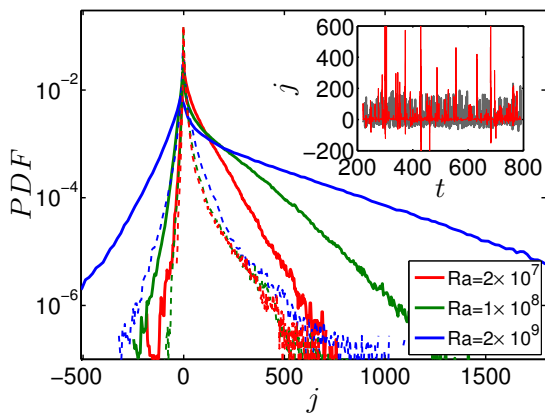


FIG. 2. PDFs of the local instantaneous heat flux j near the side wall at $r/L = 0.45$ (solid, thick lines) and near the axis $r/L = 0.06$ (dashed, thin lines) at mid-height for $Ra = 2 \times 10^7$ (red), 1×10^8 (green), 2×10^9 (blue). The inset shows time series for the heat flux near the side wall (thin, red) and in the center (thick, gray) for $Ra = 1 \times 10^8$.

to resolve the thermal boundary layers is shown in the fourth column. In a RB cell with no slip velocity condition on the walls the dimensional thermal energy dissipation rate, $\varepsilon_T = \kappa \Delta^2 L^{-2} \langle |\nabla \theta|^2 \rangle_V$ and kinetic energy dissipation rate $\varepsilon_K = \nu^3 L^{-4} Pr^{-1} Ra \langle |\nabla \mathbf{u}|^2 \rangle_V$ satisfy exact relationships with Nu (see Refs. [1, 25]), namely $\varepsilon_T = \kappa \Delta^2 L^{-2} Nu$ and $\varepsilon_K = \nu^3 L^{-4} Pr^{-2} Ra (Nu - 1)$. In order to validate our simulations the obtained energy dissipation rates are compared with Nu in Table I. These ratios are near one, which proves the adequacy of the grid resolution. In the seventh column the largest grid spacings in the azimuthal and axial directions are compared with the Kolmogorov length. In the last column the total time used for the statistical averages is shown in free fall time units (L/U). The total computational time was around 2.2×10^5 CPU hours on a Power6 computer.

We placed 1880 “numerical probes” at different ra-

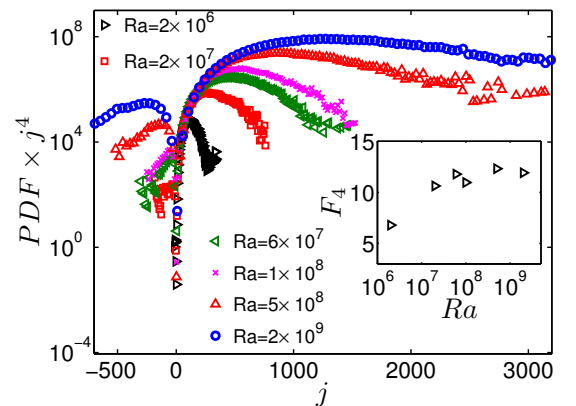


FIG. 3. $j^4 \times PDF(j)$ vs. j is shown for different Ra near the side wall region showing convergence of the flatness at that location. Note that the y-axis is given in log-scale, in contrast to the figures shown in the convergence test by Belin et al. [26], where $y^4 \times PDF(y)$ is given on a linear scale. The inset shows that the flatness F_4 increases as a function of Ra .

dial locations on three different horizontal planes (at $z/L=0.25$, $z/L=0.50$ and $z/L=0.75$), to obtain point-wise data on the temperature and vertical velocity in order to calculate the local heat flux according to equation (1). In each horizontal plane a number of azimuthally nearly equally spaced probes were placed on seven circles with radii $r/L = 0.06, 0.12, 0.19, 0.24, 0.34, 0.40$ and 0.45 , see Figure 1. On each circle we distributed 60 probes at $z/L = 0.50$ and 20 probes at $z/L = 0.25, 0.75$. In addition, on the mid-plane, each circle was complemented by two other circles, one inside and one outside, spaced by one radial mesh length as shown in the upper right corner of Figure 1. In total, we have information from 60 (azimuthal) $\times 7$ (radial) $\times 3$ (sets) = 1260 probes at mid-height plane. For the planes at $z/L = 0.25$ and at $z/L = 0.75$ we have information from $20 \times 7 = 140$ probes.

As a further check on the consistency of the calcu-

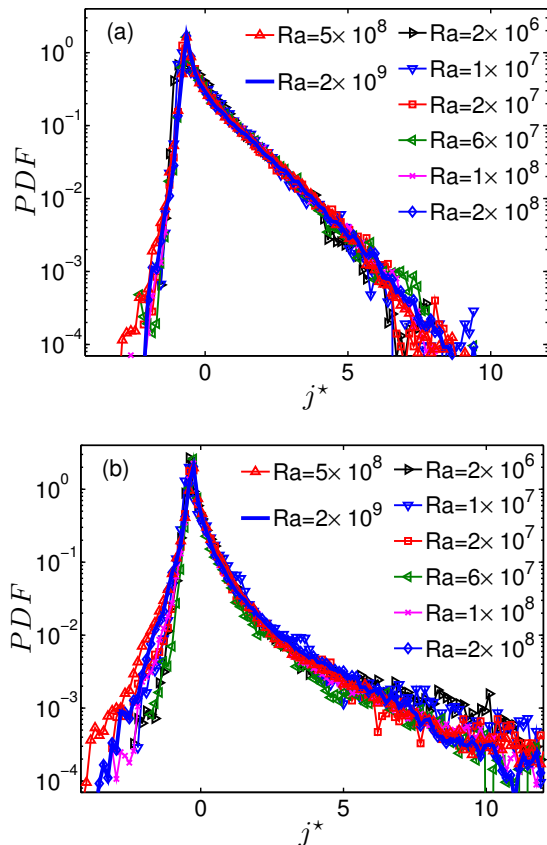


FIG. 4. Centered PDFs of the normalized heat flux $j^* = (j - \bar{j})/j_{rms}$ on the mid-plane (a) near the side wall $r/L = 0.45$, and (b) near the axis $r/L = 0.06$.

lations we compare the time- and area-averaged heat flux as monitored by all the mid-plane probes mentioned before complemented by 340 additional ones uniformly spaced in the angular direction and non-uniformly in the radial direction. For $Ra = 5 \times 10^8$ we found a global average Nusselt number of 51.58 while from the r -averaged heat flux from the probes at mid-height we found $Nu = 50.83$. Similarly, for $Ra = 2 \times 10^9$, the two results were 78.80 and 76.41. In view of the discretization error introduced by the sparseness of the numerical probes (5% of the actual computational cells on the mid-plane), this can be considered as a good agreement.

III. RESULTS

A. Local heat flux

In Figure 2 we show PDFs for the local instantaneous heat flux j on the mid-plane, at two different radial positions, one near the cell axis ($r/L = 0.06$) and one near the side wall ($r/L = 0.45$). Note that the latter is outside the kinematic boundary layer (BL) which at this Prandtl number has a thickness of $\lambda_u/L \approx 3.6Ra^{-0.26 \pm 0.03}$ [27]. According to this scaling law we have $\lambda_u/L \approx 0.05$ for $Ra = 10^7$ and $\lambda_u/L \approx 0.016$ for $Ra = 10^9$. From our

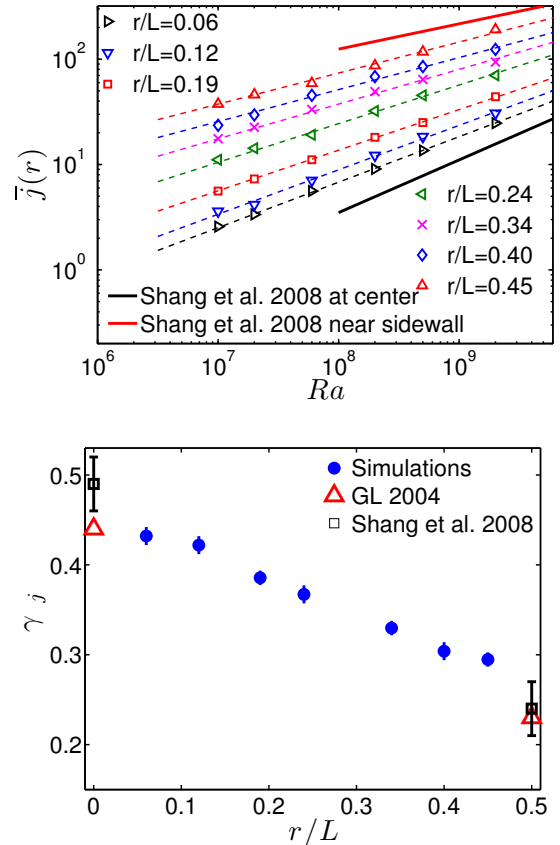


FIG. 5. (a): Open symbols indicate the numerical results for the local heat flux averaged over time and angular position as function of Ra at different radial positions r/L . The solid lines show the experimental data of Shang et al. [18]. (b): The scaling exponent for the time- and angle-averaged heat flux as function of the radial position r/L for the simulations, experiment [18], and theory [11].

numerical calculations of the kinetic side wall BL thickness, as identified by the location of the maximal velocity fluctuations, we get even slightly smaller values. Obviously, there is no thermal BL at the side walls due to the adiabatic boundary conditions.

The first striking observation from Figure 2 is that the absolute value of the heat flux is much larger at the side walls (solid lines) as compared to the center (dashed lines). This is consistent with the expectation that most of the heat is transported by the large-scale convection roll and of course it is well known [18]. In addition, we observe that the PDF close to the side walls has a positive skewness due to rising and falling of the warm and cold plumes. We observe some events with a heat flux as high as fifteen times the average. The PDF of the local heat flux in the cell center also has a positive skewness, which indicates that plumes can travel through this region as well. The inset of Figure 2 shows j as a function of the dimensionless time t close to the cell center ($r/L=0.06$) and to the side wall ($r/L=0.45$) for $Ra = 10^8$ and again reflects the presence of much stronger heat transport events near the side wall than in the center.

One of the main features of turbulence is the small

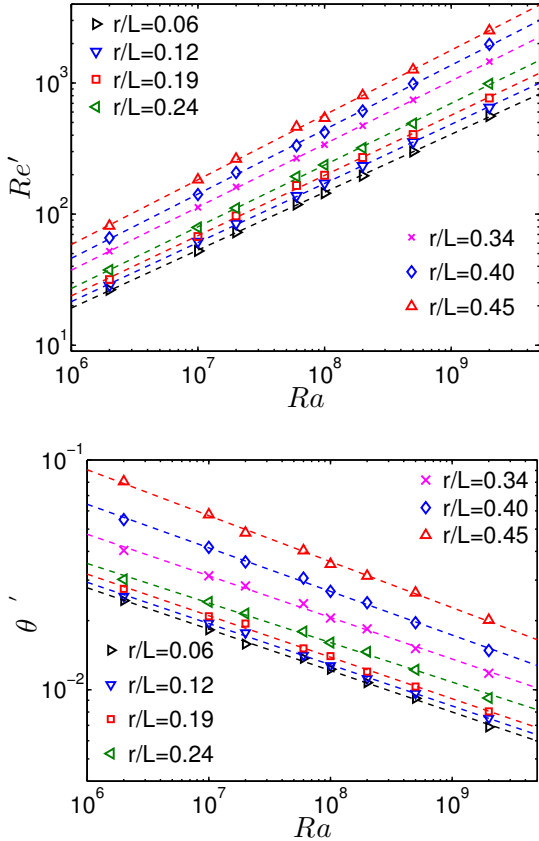


FIG. 6. Panel (a) shows the Reynolds number based on the rms velocity, Re' , and panel (b) the normalized rms temperature θ' as function of Ra ; both for different radial positions.

scale intermittency that is measured as departure from a Gaussian character of the PDF, mainly the tails and the peakedness. This can be quantified by calculating the flatness F_4 of the PDF. For strongly intermittent signals however the integral of $j^4 \times PDF(j)$ defining the flatness may not converge. To examine this issue we calculate the angular average of this quantity at $r/L = 0.06$ and at $r/L = 0.45$ on the mid-plane. While at the side wall this quantity decays for large $|j|$ sufficiently fast, see Figure 3 (this feature is more evident when data is plotted on a linear rather than log-scale), and thus permits the calculation of the flatness (showing strong intermittency, $F_4 \approx 11$, inset of Figure 3), in the center the intermittency is so strong that no convergence for the flatness can be achieved.

By rescaling the heat flux j with its standard deviation j_{rms} , the zero-mean PDF for the normalized heat flux $j^* \equiv (j - \bar{j})/j_{rms}$ shows universality near the side wall (see Figure 4a). The tails for the rescaled PDFs are shorter at the side walls compared to those at the center. This indicates relatively fewer plumes carrying a large heat flux at the side walls in contrast to relatively more plumes carrying a smaller heat flux at the center, and again underlines the extremely strong intermittency of the heat flux in the center (see Figure 4b).

Figure 5a shows the time- and angularly-averaged heat flux as a function of Ra at different radial positions on

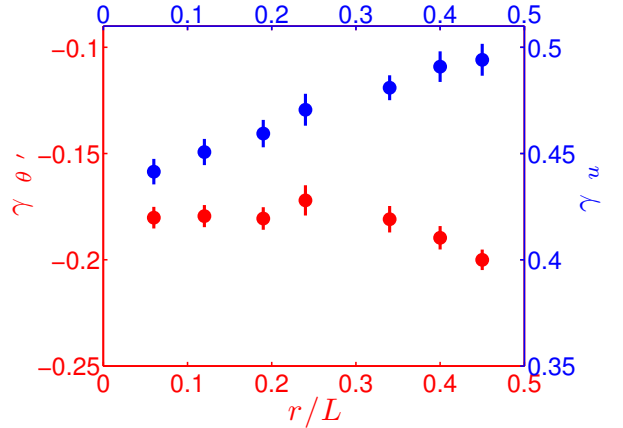


FIG. 7. The variations in the velocity and temperature scaling exponents with Ra are shown as functions of the radial position.

the mid-plane. Figure 5b shows that the corresponding scaling exponent γ_j as a function of the radial position decreases monotonically from 0.43 near the axis to 0.29 close to the side wall. The measurements of Shang et al. [18] and the theoretical analysis of Grossmann and Lohse [11] only made statements on the values close to the side wall and to the axis; these are well confirmed by the present results. In the Ra range considered here the heat transport near the side wall is an order of magnitude larger than in the center. An extrapolation of the power law fits $\bar{j} = 0.0025Ra^{0.43 \pm 0.01}$ obtained near the center and $\bar{j} = 0.3236Ra^{0.29 \pm 0.01}$ valid near the wall, shows that these become equal for $Ra \approx 10^{15}$. This value is consistent with the prediction of the unifying theory [9]. Recent experiments [28] suggests the occurrence of this feature in the range $10^{13} \leq Ra \leq 5 \times 10^{14}$, whereas Shang et al. [18] suggested that it happens at $Ra \approx 10^{14}$, based on their extrapolation.

B. Local fluctuations

In this section, we determine the scaling with Ra of the velocity and temperature fluctuations with respect to their global mean at different radial locations. Since the global mean of the vertical velocity vanishes, to characterize the velocity fluctuations u_{rms} it is sufficient to take the root mean square of the fluid velocity at each position and average it in the azimuthal direction. Figure 6a shows $Re' \equiv \sqrt{(Ra/Pr)}u_{rms}$ (equivalent to $U_{dim}L/\nu$ with U_{dim} the dimensional rms velocity) as a function of Ra on the mid-plane.

For the normalized temperature fluctuations we take the root mean square of $\theta' = \theta - 1/2$. Figure 6b shows the results for this quantity vs. Ra at different radial positions on the mid-plane. At all radial positions, fluctuations of both velocity and temperature exhibit a power law dependence on Ra proportional to Ra^{γ_u} and $Ra^{\gamma_{\theta'}}$,

TABLE II. Summary of the velocity and temperature scaling exponents γ_u and γ_θ reported in several experimental (E) and theoretical (T) studies. The experiments mentioned below have been carried out in cylindrical cells, unless stated otherwise.

	Ra	Pr	Γ	γ_u (center)	γ_θ (center)	γ_u (side wall)	γ_θ (side wall)
Castaing et al. [29] (E)	$4 \times 10^7 - 6 \times 10^{12}$	0.65 – 1.5	1	0.491 ± 0.002	-0.147 ± 0.005	–	–
Castaing et al. [29] (T)	$4 \times 10^7 - 6 \times 10^{12}$	0.65 – 1.5	1	3/7	-1/7	–	–
Sano et al. [30] (E)	$10^8 - 10^{10}$	0.64 – 1.4	1	–	–	0.485 ± 0.005	–
Takeshita et al. [31] (E)	$10^6 - 10^8$	0.024	1	–	–	0.46 ± 0.02	–
Ashkenazi et al. [32, 33] (E)	$10^{11} - 5 \times 10^{14}$	27 – 190	1 (square)	–	–	0.43 ± 0.02	–
Chavanne et al. [34] (E)	$10^7 - 6 \times 10^{12}$	0.7 – 4	0.5	–	–	0.49	–
Daya and Ecke [35] (E)	$2 \times 10^8 - 4 \times 10^9$	5.46	0.79	0.5 ± 0.03	-0.10 ± 0.02	–	–
Niemela et al. [36] (E)	$15 \times 10^6 - 10^{13}$	0.7	1	–	–	0.5	–
Qiu et al. [37, 38] (E)	$10^8 - 10^{10}$	5.4 – 5.5	1	0.55	–	0.46	–
Lam et al. [39] (E)	$10^6 - 10^{11}$	6 – 1027	0.5 – 4.4	–	–	0.495 (bottom)	–
Grossman and Lohse [11] (T)	$10^6 - 10^{14}$	$\sim 0.1 - 10$	1	0.34	-0.11 to -0.16	–	-0.09 to -0.11
Shang et al. [18] (E)	$10^8 - 10^{10}$	4.4	1	0.49 ± 0.03	-0.14 ± 0.03	0.46 ± 0.03	-0.24 ± 0.03
Present work	$2 \times 10^6 - 2 \times 10^9$	5.2	1	0.44 ± 0.01	-0.18 ± 0.01	0.49 ± 0.01	-0.20 ± 0.01

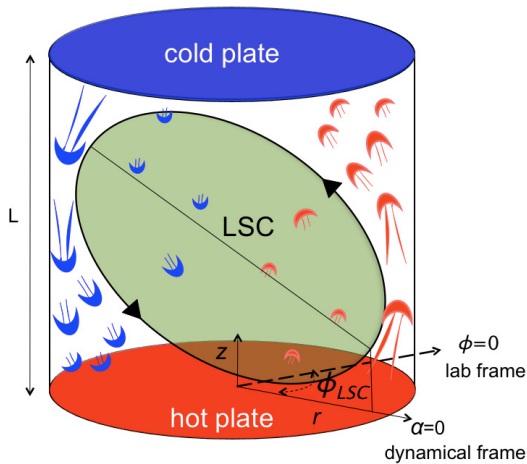


FIG. 8. Sketch of the LSC in a cylindrical RB cell. The warm plumes go upwards on the right side, defined as $\alpha = 0$, and go downwards on the left side of the cell, defined as $\alpha = \pi$. Due to the shape of the LSC the warm uprising fluid (cold down flowing fluid) is close to the side wall at $z/L = 0.25$ and $z/L = 0.50$ ($z/L = 0.75$ and $z/L = 0.50$).

respectively. In this Ra number regime the thermal fluctuations close to the side wall are an order of magnitude larger than at the cell center due to the plumes that travel along the wall. Figure 7 shows that the corresponding velocity scaling exponents increase smoothly from $\gamma_u = 0.44$ in the cell center to $\gamma_u = 0.49$ near the side wall. Figure 7 shows that the corresponding temperature scaling exponent decreases from $\gamma_\theta = -0.18$ in the cell center to $\gamma_\theta = -0.20$ near the side wall.

Table II summarizes the data for the scaling exponents available in the literature and compares them with the present ones. There are some differences among the values reported. This is due in part to the spatial dependence of this quantity, shown in Figure 7, but also to the use of different experimental techniques which measure somewhat different quantities. Overall, there is a general consistency among the data shown. The origin of the

residual differences cannot be ascertained on the basis of the presently available knowledge and must await further research.

IV. STATISTICS WITH RESPECT TO THE ORIENTATION OF THE LARGE SCALE CIRCULATION

For $\Gamma = 1$, the flow in the cell is characterized by a large scale circulation (LSC) [30, 40–42] as sketched in Figure 8. Most of the plumes travel in the LSC plane close to the side wall. In experiments the LSC orientation can be detected with thermistors embedded in the side wall [43] which measure relatively higher and lower temperatures in the region of upflow and downflow [42]. Here we want to determine how the local heat flux depends on the location of measurement with respect to the LSC orientation plane.

A. Determination of LSC orientation

We know from Ref. [44] that, in the present range of Ra numbers, the period of the LSC is approximately 10 dimensionless time units. On this basis, according to the last column of Table 1, our simulations are long enough to cover more than 400 LSC periods for the smallest Ra and 175 for the highest one.

To determine the LSC orientation we use cosine fits of vertical velocity, temperature and heat flux over horizontal planes in the angular direction near the side wall at $r/L = 0.45$. For this purpose we use the information from the numerical probes placed uniformly in this direction (see section 2) [42, 45]. In performing the fits we need to take into account that the orientation of the LSC plane changes with time. To this end we have pre-processed the instantaneous data by filtering them by means of short-time moving averages of four different durations, namely 4, 10, 20 and 50 dimensionless time units. We have fitted the results of each one of these time averages by an

expression of the form

$$f_i = f_m + A_f \cos(m\phi_i + \phi_{LSC}), \quad (4)$$

where f_i is the (short-time moving averaged) information provided by the i^{th} probe at the angular position ϕ_i , f_m is the angular mean value, A_f is the amplitude of the fit and ϕ_{LSC} is the phase shift with respect to the reference frame of the computation; the integer m equals 1 or 2 depending on the angular periodicity of the quantity f as will be clear below.

An example of the difference between instantaneous and short-time-averaged data for the heat flux j is shown in the top panel of Figure 9 for $Ra = 2 \times 10^8$ on the mid-plane of the cylinder. The dashed line is the result of the fit to a portion of the instantaneous data averaged for 20 dimensionless time units. The bottom panel of Figure 9 shows the filtered data and their cosine fit for the vertical velocity for the same positions and interval of time used for the top panel. The maximum of the curve is marked with a red cross and identifies the position of the LSC plane. A graph showing ϕ_{LSC} vs. time as calculated using the four different averaging times is shown in Figure 10. As expected, the fluctuations in the position of the LSC plane are somewhat greater when short averaging times are used.

Once the position of the LSC plane is known, all the short time averages can be referred to it by using a new angular co-ordinate $\alpha = \phi - \phi_{LSC}$. With this construction, the same value of α in each filtered segment of data identifies the same position relative to the LSC and justifies taking the average over all the filtered data sets. Such averages for the vertical velocity and heat flux at $r/L = 0.45$ on the mid-plane are shown in Figure 11. A comparison of the two panels in this figure shows that the heat flux has double the periodicity of the velocity (i.e. the integer m in equation (4) equals 2 as opposed to $m = 1$ for the velocity), because the heat flux is enhanced in correspondence of both the upward and downward moving streams of the LSC. The local heat flux is lower in the areas where the LSC is not present.

The panel with the heat flux in Figure 11 actually contains four different sets of symbols, each one denoting the results obtained with a different averaging time. The virtual coincidence of these four sets demonstrates the robustness of the results with respect to the filtering time used.

In Figure 12 the amplitudes of the cosine fits for temperature, A_θ , axial velocity, A_{u_z} , and normalized heat flux, A_j are shown as functions of Ra at mid-height near the side wall, $r/L = 0.45$. Interestingly, these amplitudes have a power-law dependency on Ra , with scaling exponents -0.250 ± 0.010 , 0.020 ± 0.005 , 0.019 ± 0.005 for temperature, axial velocity and local heat flux respectively.

Figure 13a shows the time-averaged local heat flux as a function of Ra at different α at mid-height near the side wall. From the figure it is clear that the local heat flux

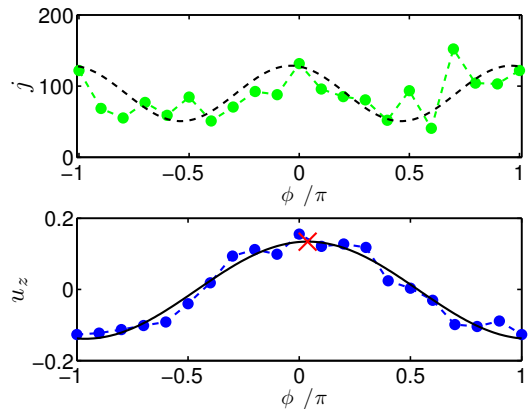


FIG. 9. Angular dependencies of heat flux and vertical velocity on the mid-plane at $r/L = 0.45$ near the side wall for $Ra = 2 \times 10^8$: (a) instantaneous local heat flux (green points), (b) vertical velocity (blue points). The orientation of the LSC plane is determined by using the filtered time average of 20 dimensionless time units on vertical velocity data and the best cosine fit is shown in black solid line. The red cross indicates the maximum of the cosine fit, which we take as the LSC orientation.

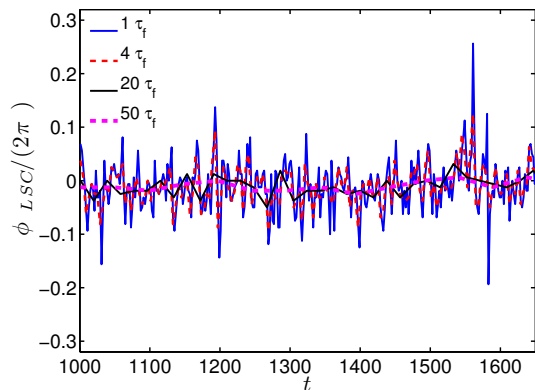


FIG. 10. LSC orientation as function of time for $Ra = 2 \times 10^8$. The time averaging that is applied to the signal before the analysis is 1 (blue-solid), 4 (red-dashdot), 20 (black-solid) and 50 (magenta-dash) dimensionless time units.

has a power law dependence on Ra . In agreement with the data in Figure 12 we find that the local heat flux at the LSC orientation increases faster than in the regions away from LSC. This is also revealed when the local heat flux scaling exponent as function of α , see Figure 13b, is considered.

Figure 14 shows the variation of the time-averaged local heat flux with α at three different heights. For $z/L = 0.25$ larger values of j occur near $\alpha = 0$, and lower values near $\alpha = \pi$. A similar picture shifted by π is found for $z/L = 0.75$, with higher values near $\alpha = \pi$ and lower values near $\alpha = 0$. At $z/L = 0.50$, on the other hand, the levels at $\alpha = 0$ and $\alpha = \pi$ are comparable. These results suggest that the plane of the LSC is

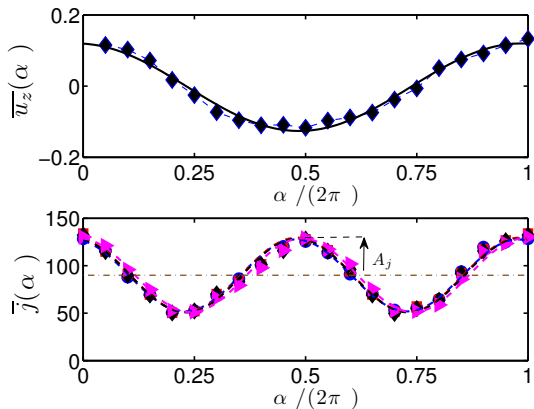


FIG. 11. Time averaged quantities relative to the orientation of the LSC plane near the side walls ($r/L = 0.45$) at mid-height: (a) vertical velocity averaged over 20 dimensionless time units; (b) local heat flux $\overline{j}(\alpha)$ averaged over 4 (circle-blue), 10 (square-red), 20 (diamond-black) and 50 (triangle-magenta) dimensionless time units. The best cosine fit, with a period of 4π which corresponds to $m = 2$ in (4), is shown by dashes. The mean heat flux (thin-dash dot) and the amplitude of variation A_j are also shown. The hot plumes originate in the neighborhood of $\alpha = 0$.

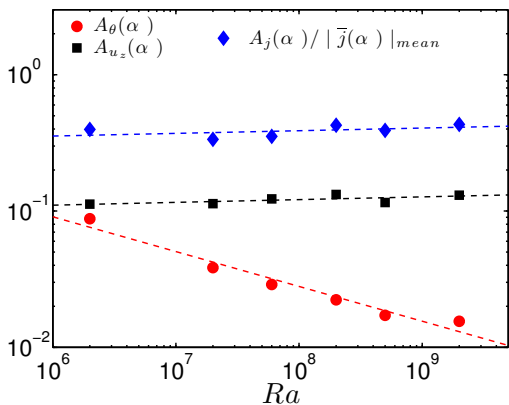


FIG. 12. The amplitude variation of cosine fits near the side walls, $r/L = 0.45$, at the mid-height as function of Ra . The data are shown for temperature (circle-red), axial velocity (square-black) and normalized heat flux (diamond-blue). Here $|\overline{j}(\alpha)|_{mean}$ is the arithmetic mean heat flux in the azimuthal direction for a given Ra . The dashed lines indicates the power law fits for the data.

tilted as sketched in Figure 8. This feature has also been found in experiments of Funfschilling et al. [46].

V. SUMMARY AND CONCLUSIONS

To summarize, we investigated numerically the scaling of the local heat flux in Rayleigh-Bénard convection of a fluid with $Pr = 5.2$ (appropriate for water at 32°C) for $2 \times 10^6 \leq Ra \leq 2 \times 10^9$ in a unit aspect ratio cylinder. In this Ra number regime the local heat flux is larger

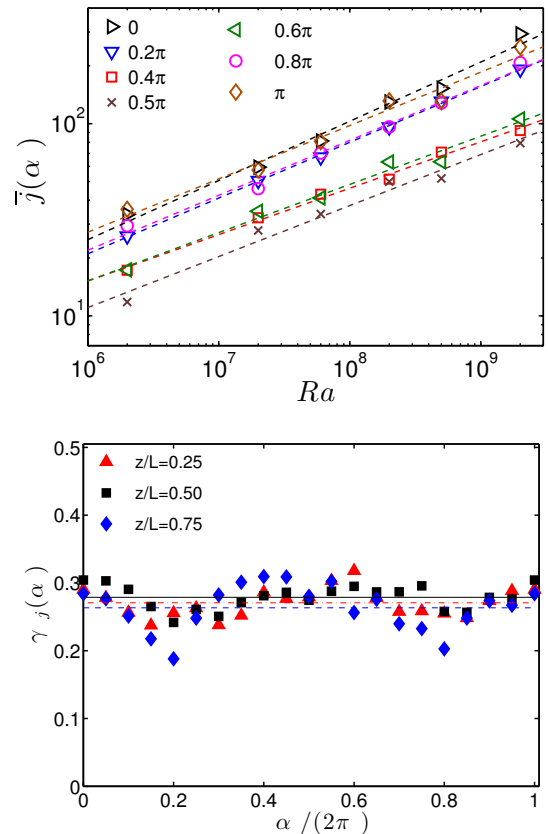


FIG. 13. (a): Scaling of the time averaged local heat flux with Ra near the side walls, $r/L = 0.45$, at mid-height. The symbols indicate measurements taken at different α . The dashed lines are the power law fits to the data. (b): Scaling exponent for the heat flux $\gamma_j(\alpha)$ relative to the LSC plane near the side wall, $r/L = 0.45$ at $z/L = 0.25$ (triangles-red), $z/L = 0.50$ (square-black), and $z/L = 0.75$ (diamond-blue). The straight lines indicate the arithmetic mean values of the scaling exponents.

close to the side wall than on the axis. The local heat flux $u_z(T - T_0)$ is a positive quantity both when fluid warmer than the average temperature T_0 rises and fluid colder than T_0 sinks. The PDFs of the local heat flux have a positive skewness due to the dominance of plume transport in this Ra range. On the mid-plane, the scaling exponents of the local heat flux with Ra near the axis and close to the side wall agree well with the measurements of Shang et al. [18] and the predictions of Grossmann and Lohse [11]. Here we have shown that these scaling exponents decrease monotonically with position r from 0.43 near the axis to 0.29 close to the side wall. The scaling exponent for the Reynolds number based on the rms velocity depends on the radial position as well, with a value of 0.44 near the axis and 0.49 close to the side wall. For the scaling exponents of the temperature fluctuations we find -0.18 and -0.20 respectively. We showed the marked effect of the LSC which causes local heat fluxes more than twice as large in its plane than at 90° from it. This effect becomes stronger for high Ra .

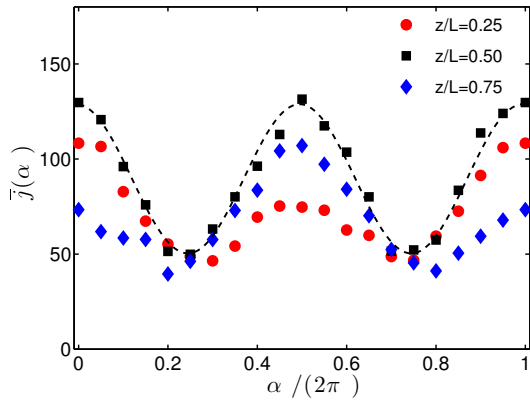


FIG. 14. Time averaged local heat flux with respect to the LSC orientation for $Ra = 2 \times 10^8$ at different axial positions for $r/L = 0.45$. The points are, near the hot plate $z/L = 0.25$ (circle-red), at mid-height $z/L = 0.50$ (square-black), and near the top plate $z/L = 0.75$ (diamond-blue). Moving averages are taken over 30 dimensionless time units.

ACKNOWLEDGEMENTS

We acknowledge the financial support by the Foundation for Fundamental Research on Matter (FOM) and the National Computing Facilities (NCF), both sponsored by NWO. This research is a part of industrial partnership program on Fundamentals of Heterogeneous Bubbly Flows (FHBF). The computations in this project have been performed on Huygens cluster of SARA in Amsterdam.

-
- [1] G. Ahlers, S. Grossmann, and D. Lohse, *Heat transfer and large scale dynamics in turbulent Rayleigh-Bénard convection*, Rev. Mod. Phys. **81**, 503 (2009).
- [2] D. Lohse and K. Q. Xia, *Small-scale properties of turbulent Rayleigh-Bénard convection*, Ann. Rev. Fluid Mech. **42**, 335 (2010).
- [3] E. D. Siggia, *High Rayleigh Number convection*, Annu. Rev. Fluid Mech. **26**, 137 (1994).
- [4] S. Grossmann and D. Lohse, *Scaling in thermal convection: A unifying view*, J. Fluid. Mech. **407**, 27 (2000).
- [5] K. Q. Xia, S. Lam, and S. Q. Zhou, *Heat flux measurement in high Prandtl number turbulent Rayleigh-Bénard convection*, Phys. Rev. Lett. **88**, 064501 (2002).
- [6] A. Nikolaenko, E. Brown, D. Funfschilling, and G. Ahlers, *Heat transport by turbulent Rayleigh-Bénard convection in cylindrical cells with aspect ratio one and less*, J. Fluid Mech. **523**, 251 (2005).
- [7] D. Funfschilling, E. Brown, A. Nikolaenko, and G. Ahlers, *Heat transport by turbulent Rayleigh-Bénard convection in cylindrical samples with aspect ratio one and larger*, J. Fluid Mech. **536**, 145 (2005).
- [8] C. Sun, L. Y. Ren, H. Song, and K. Q. Xia, *Heat transport by turbulent Rayleigh-Bénard convection in 1 m diameter cylindrical cells of widely varying aspect ratio*, J. Fluid Mech. **542**, 165 (2005).
- [9] S. Grossmann and D. Lohse, *Thermal convection for large Prandtl number*, Phys. Rev. Lett. **86**, 3316 (2001).
- [10] S. Grossmann and D. Lohse, *Prandtl and Rayleigh number dependence of the Reynolds number in turbulent thermal convection*, Phys. Rev. E **66**, 016305 (2002).
- [11] S. Grossmann and D. Lohse, *Fluctuations in turbulent Rayleigh-Bénard convection: The role of plumes*, Phys. Fluids **16**, 4462 (2004).
- [12] X. D. Shang, X. L. Qiu, P. Tong, and K. Q. Xia, *Measured local heat transport in turbulent Rayleigh-Bénard convection*, Phys. Rev. Lett. **90**, 074501 (2003).
- [13] Y. Gasteuil, W. L. Shew, M. Gibert, F. Chillá, B. Castaing, and J. Pinton, *Lagrangian temperature, velocity, and local heat flux measurement in Rayleigh-Bénard convection*, Phys. Rev. Lett. **99**, 234302 (2007).
- [14] J. Schumacher, *Lagrangian dispersion and heat transport in convective turbulence*, Phys. Rev. Lett. **100**, 134502 (2007).
- [15] X. D. Shang, X. L. Qiu, P. Tong, and K. Q. Xia, *Measurements of the local convective heat flux in turbulent Rayleigh-Bénard convection*, Phys. Rev. E **70**, 026308 (2004).
- [16] The diffusive heat flux $-\kappa \overline{\partial_z T}(r, t) / (\kappa \Delta / L)$ is less than 1% of the convective one, for all r and Ra , due to the tiny temperature gradient at mid height.
- [17] E. S. C. Ching, H. Guo, X. D. Shang, P. Tong, and K. Q. Xia, *Extraction of plumes in turbulent thermal convection*, Phys. Rev. Lett. **93**, 124501 (2004).
- [18] X. D. Shang, P. Tong, and K. Q. Xia, *Scaling of the local convective heat flux in turbulent Rayleigh-Bénard convection*, Phys. Rev. Lett. **100**, 244503 (2008).
- [19] D. Lohse and F. Toschi, *The ultimate state of thermal convection*, Phys. Rev. Lett. **90**, 034502 (2003).
- [20] R. Verzicco and R. Camussi, *Numerical experiments on strongly turbulent thermal convection in a slender cylindrical cell*, J. Fluid Mech. **477**, 19 (2003).
- [21] P. Orlandi, *Fluid flow phenomena: A numerical tool kit* (Kluwer academic publishers, Dordrecht, The Netherlands, 2001).
- [22] R. Verzicco and P. Orlandi, *A finite-difference scheme for three-dimensional incompressible flows in cylindrical coordinates*, J. Comp. Phys. **123**, 402 (1996).
- [23] R. Verzicco and R. Camussi, *Transitional regimes of low-Prandtl number thermal convection in a cylindrical cell*, Phys. Fluids **1287** (1997).
- [24] R. J. A. M. Stevens, R. Verzicco, and D. Lohse, *Radial boundary layer structure and Nusselt number in Rayleigh-Bénard convection*, J. Fluid Mech. **643**, 495 (2010).

- [25] B. I. Shraiman and E. D. Siggia, *Heat transport in high Rayleigh number convection*, Physical Review A **42-6**, 3650 (1990).
- [26] F. Belin, P. Tabeling, and H. Willaime, *Exponents of the structure functions in a low temperature helium experiment*, Physica D, Nonlinear Phenomena **93(1-2)**, 5263 (1996).
- [27] X. L. Qiu and K. Q. Xia, *Viscous boundary layers at the side wall of a convection cell*, Phys. Rev. E **58**, 486 (1998).
- [28] X. He, Funfschilling, E. Nobach, E. Bodenschatz, and G. Ahlers, *Transition to the ultimate state of turbulent Rayleigh-Bénard convection*, Phys. Rev. Lett. **108**, 024502 (2012).
- [29] B. Castaing, Gunaratne, G. Heslot, L. F. Kadanoff, A. Libchaber, A. S. Thomae, X. Z. Wu, S. Zaleski, and G. Zanetti, *Scaling of hard thermal turbulence in Rayleigh-Bénard convection*, J. Fluid Mech. **204**, 1 (1989).
- [30] M. Sano, X.-Z. Wu, and A. Libchaber, *Turbulence in helium-gas free convection*, Phys. Rev. A **40**, 6421 (1989).
- [31] T. Takeshita, T. Segawa, J. Glazier, and M. Sano, *Thermal turbulence in Mercury*, Phys. Rev. Lett. **76**, 1465 (1996).
- [32] S. Ashkenazi and V. Steinberg, *Spectra and statistics of velocity and temperature fluctuations in turbulent convection*, Phys. Rev. Lett. **83**, 4760 (1999).
- [33] S. Ashkenazi and V. Steinberg, *High Rayleigh number turbulent convection in a gas near the gas-liquid critical point*, Phys. Rev. Lett. **83**, 3641 (1999).
- [34] X. Chavanne, F. Chilla, B. Chabaud, B. Castaing, and B. Hebral, *Turbulent Rayleigh-Bénard convection in gaseous and liquid He*, Phys. Fluids **13**, 1300 (2001).
- [35] Z. A. Daya and R. E. Ecke, *Does turbulent convection feel the shape of the container?*, Phys. Rev. Lett. **87**, 184501 (2001).
- [36] J. Niemela, L. Skrbek, K. R. Sreenivasan, and R. J. Donnelly, *The wind in confined thermal turbulence*, J. Fluid Mech. **449**, 169 (2001).
- [37] X. L. Qiu and P. Tong, *Temperature oscillations in turbulent Rayleigh-Bénard convection*, Phys. Rev. E **66**, 026308 (2002).
- [38] X. L. Qiu, X.-L. Shang, P. Tong, and K. Q. Xia, *Velocity oscillations in turbulent Rayleigh-Bénard convection*, Phys. Fluids **16**, 412 (2004).
- [39] S. Lam, X. D. Shang, S. Q. Zhou, and K. Xia, *Prandtl-number dependence of the viscous boundary layer and the Reynolds number in Rayleigh-Bénard convection*, Phys. Rev. E **65**, 066306 (2002).
- [40] R. Krishnamurti and L. Howard, *Large scale flow generation in turbulent convection*, Proc. Nat. Acad. Sci. USA **78(4)**, 1981 (1981).
- [41] K.-Q. Xia, C. Sun, and S.-Q. Zhou, *Particle image velocimetry measurement of the velocity field in turbulent thermal convection*, Phys. Rev. E **68**, 066303 (2003).
- [42] E. Brown and G. Ahlers, *The origin of oscillations of the large-scale circulation of turbulent Rayleigh-Bénard convection*, J. Fluid Mech **638**, 383 (2009).
- [43] E. Brown, A. Nikolaenko, and G. Ahlers, *Reorientation of the large scale circulation in turbulent Rayleigh-Bénard convection*, Phys. Rev. Lett. **95**, 084503 (2005).
- [44] J. B. Cuba, M. S. Emran, and J. Schumacher, *Aspect ratio dependence of heat transfer and large scale flow in turbulent convection*, J. Fluid Mech. **655**, 152 (2010).
- [45] R. J. A. M. Stevens, H. J. H. Clercx, and D. Lohse, *Effect of plumes on measuring the large scale circulation in turbulent Rayleigh-Bénard convection*, Phys. Fluids **23**, 095110 (2011).
- [46] D. Funfschilling, E. Brown, and G. Ahlers, *Torsional oscillations of the large-scale circulation in turbulent Rayleigh-Bénard convection*, J. Fluid Mech. **607**, 119139 (2008).